Synthesis and Characterization of Ultrathin WO₃ Nanodisks Utilizing Long-Chain Poly(ethylene glycol)†

Abraham Wolcott,‡ Tev R. Kuykendall,§ Wei Chen,‡ Shaowei Chen,‡ and Jin Z. Zhang*,‡

Department of Chemistry and Biochemistry, University of California, Santa Cruz, California 95064, and Department of Chemistry and Biochemistry, University of California, Berkeley, California 94720

Received: July 26, 2006; In Final Form: October 2, 2006

Metal oxide nanostructures hold great potential for photovoltaic (PV), photoelectrochemical (PEC), and photocatalytic applications. Whereas thin films of various materials of both nanoparticle and nanorod morphologies have been widely investigated, there have been few inquiries into nanodisk structures. Here, we report the synthesis of ultrathin WO₃ nanodisks using a wet chemical route with poly(ethylene glycol) (PEG) as a surface modulator. The reported nanodisk structure is based on the interaction of the nonionic 10000 g/mol PEG molecules with tungsten oxoanion precursors. The WO₃ nanostructures formed are dominated by very thin disks with dimensions on the nanometer to micrometer scale. Scanning electron microscopy (SEM) and transmission electron microscopy (TEM) images reveal the structures to have dimensions on the order of 350−1000 nm in length, 200−750 nm in width, and 7−18 nm in thickness and possessing textured single-crystalline features. A number of analytical techniques were used to characterize the WO₃ nanodisks, including selected-area electron diffraction (SAED), X-ray diffraction (XRD), energy-dispersive X-ray spectroscopy (EDX), atomic force microscopy (AFM), Raman scattering spectroscopy, UV−visible spectrophotometry, and cyclic voltammetry (CV). The growth of the WO₃ nanodisks was inhibited in the [010] crystal direction, leading to ultrathin morphologies in the monoclinic crystal phase. The large flat surface area and high aspect ratio of the WO₃ nanodisks are potentially useful in PEC cells for hydrogen production via direct water splitting, as has been demonstrated in a preliminary experiment with external bias.

1. Introduction

Recent revelations of the increase in greenhouse gases (CO₂ and CH₄) in the atmosphere highlight the concern over global warming and the human impact on our environment.[1] More directly, it emphasizes the need to reduce the amount of fossil fuel combustion, the leading cause of greenhouse gas emission. Renewable energy technologies such as solar, fuel cell, and wind are sustainable and economically viable alternatives to fossil fuels.[2] Utilization of all available renewable energy technologies will be the most pragmatic solution to the world's energy needs in the future. One of the most egalitarian energy sources is hydrogen generation via solar radiation utilizing photoelectrochemical (PEC) cells. Khaselev and Turner demonstrated its feasibility with a fully integrated photovoltaic−photoelectrochemical (PV−PEC) device with 12.4% photon-to-hydrogen conversion efficiency.[3]

Advances in semiconductor and metal oxide nanomaterials for PV cells and direct water splitting via photolysis have highlighted the inherent advantages of manipulating structures on the nanoscale.[4,5] Dye-sensitized nanocrystalline TiO₂ photovoltaic cells (Graetzel cells) have garnered the most attention in the renewable energy campaign with photon-to-current efficiencies of 10% and higher.[6] Modifications to the TiO₂ system with gold nanoparticles resulted in higher photocurrents (3-fold increase) because of increased charge-transfer dynamics explained principally by greater charge separation within the TiO₂ matrix.[7] Park et al. constructed Pt/TiO₂ PEC arrays for direct hydrogen generation with a solar-to-hydrogen efficiency of 2.2% and with 88% solar-to-electrical conversion efficiency.[8] Principally, TiO₂[8] and ZnO[9] systems utilized for solar cell applications are typically spheroid, but 1-D nanostructures have also been investigated for their light-harvesting capabilities. Nanorod systems of ZnO, Fe₂O₃, and TiO₂ have been investigated as both solar cells and PEC cells, and core−shell InP−CdS and InP−ZnTe have been theoretically proposed as PEC materials.[10−13]

Historically, 0-D (quantum dot) and 1-D (nanorod) nanostructures have received significant attention over the past 10 years, whereas 2-D nanostructures (e.g., nanodisks) have been the subject of significantly fewer investigations.[14−18] Previous work with WO₃ has produced spherical nanoparticle and nanorod/nanobelt thin films on various substrates via laser ablation, sol−gel, and vapor deposition techniques.[19−22] A general method for nanorod oxides using carbon nanotubes was also applied to WO₃, but it produced low yields with tungstic acid (WO₃·2H₂O) as the tungsten source.[23] Wet chemical routes for thin films have the advantages of employing simple synthetic methods, inexpensive experimental setups and are typically scalable for industrial production. Recently, Zou et al. exploited poly(ethylene glycol) (PEG) with a molecular weight of 20000 g/mol to produce magnetic Fe₃O₄ nanodisks from ferrocene precursors through a solvothermal route.[24] So far, to our

---

knowledge, there have been no reports on WO$_3$ nanodisk structures and associated photoelectrochemical properties.

Utilization of PEG as a directing agent for crystal growth of WO$_3$ nanoparticle thin films has been well-established.[25] Santato et al. utilized Raman scattering spectroscopy and found increased crystallinity of WO$_3$·2H$_2$O colloidal solutions when PEG (PEG-300, ca. 7 repeating units) was added as a surface modulator. Comparisons of tungstic acid with PEG-300 showed Raman vibrational peaks representative of a metastable hexagonal phase with sintering at 200 °C, whereas solutions of tungstic acid without PEG-300 were discovered to be amorphous at the same annealing temperatures. The PEG modified 20−50 nm WO$_3$ nanoparticles were consequently found to have a preferential crystal growth pattern in the (200), (020), and (002) crystal faces.[25] High-molecular-weight PEG-6000 was also used as a surface modulator with WO$_3$·2H$_2$O solutions and produced WO$_3$ stacked platelets for NO$_2$ gas-sensing applications.[26] Our investigation reinforces the significant impact on the crystallographic and morphological characteristics of WO$_3$ nanostructures via PEG interactions with colloidal tungstic acid.

Here, we demonstrate a method to produce surface-modulator-driven WO$_3$ nanodisk thin films, based on long-chain PEG-10000. Scanning electron microscopy (SEM) and transmission electron microscopy (TEM) were used to characterize the nanodisks, and the crystal structure was found to be of the monoclinic WO$_3$ crystal phase. The crystal growth was inhibited in the [010] direction and produced nanodisks that were 9−24 unit cells thick. The WO$_3$ nanodisks were found to be a textured single-crystalline phase via high-resolution TEM (HRTEM), and selected-area electron diffraction (SAED) revealed a diffraction spot pattern representative of single-domain nanostructures. X-ray diffraction (XRD) data reinforce the monoclinic crystal structure, but unlike in other powder and nanocrystalline diffraction studies, the (120) had an unusually high intensity in comparison to other monoclinic WO$_3$ morphologies.[21,25,27] The WO$_3$ nanodisks were found to be impurity-free via energy-dispersive X-ray spectroscopy (EDX) measurements, and atomic force microscopy (AFM) images revealed that their orientation was slightly tilted (∼15°) from the fluorine tin oxide (FTO) substrate. Raman scattering spectra showed the characteristic vibrational modes of monoclinic WO$_3$ at 713 and 804 cm^{-1} representative of O−W−O stretching modes. Cyclic voltammetry (CV) was performed, and cathodic and anodic peaks due to H$^+$ and Na$^+$ intercalation into the WO$_3$ matrix under UV illumination were seen in the potential range between −0.4 and −0.6 V. At higher reductive potentials (between about −0.8 and −1.2 V), inefficient hydrogen gas evolution was also observed. A model is proposed to explain the growth mechanism of the WO$_3$ nanodisks via the interaction of PEG-10000 and WO$_3$·2H$_2$O precursors.

2. Materials and Methods

A. Chemicals and Materials. Sodium tungsten oxide dihydrate (Na$_2$WO$_4$·2H$_2$O, #36489-ACS) of >99% purity was purchased from Alfa-Aesar (Ward Hill, MA). Rexyn 101 proton-exchange resin (R231-500), platinum wire (#13-766-6A), and monobasic potassium phosphate (KH$_2$PO$_4$; BP362-500, 99.0%) were purchased from Fisher Scientific (Pittsburgh, PA). A liquid chromatography column (C4169) with dimensions of 10 cm by 1.5 cm and the surfactant Triton X-100 (9002-93-1) was purchased from Sigma-Aldrich (Milwaukee, WI). Poly(ethylene glycol) (PEG #30,902-8) with a molecular weight of 10000 g/mol was purchased from Aldrich (St. Louis, MO). White quartz sand (#61235-500), sodium perchlorate (NaClO$_4$; #7601-

89-0, 98%), and potassium phosphate dibasic trihydrate (HK$_2$-PO$_4$·3H$_2$O; #16788-57-1, >99%) were purchased from Acros (Pittsburgh, PA). F/SnO conducting glass was purchased from Hartford glass company (Hartford City, IN). Ag/AgCl reference electrodes were purchased from CH Instruments (Austin, TX), and high-purity silver conducting paint was obtained from Structure Probe, Inc. (SPI, West Chester, PA). A Leister heat gun was purchased from Leister (Sarnen, Switzerland).

B. WO$_3$ Nanodisk and Electrode Protocol. WO$_3$ nanodisks were prepared via a modified wet chemical route, followed by deposition onto conducting glass and sintering at 500 °C.[28] Spherical WO$_3$ particles of 30−50-nm diameter were seen by Wang et al. and Santato et al. utilizing low-molecular-weight PEG (carbawax) as a surface modulator in previous work.[21,29] Here, we found that high-molecular-weight PEG of 10000 g/mol with an approximate length of 67 nm produced consistently planar structures aligned with the surface of the F:SnO conducting glass. First, a 0.25 M solution of Na$_2$WO$_4$ was produced by dissolving 0.8225 g of Na$_2$WO$_4$ in 10 mL of Milli-Q water, then vortexing the mixture for several minutes, and finally allowing the Na$_2$WO$_4$ to dissolve. A 10 cm by 1.5 cm liquid chromatography column was packed with proton-exchange resin, a 0.2 cm layer of white quartz sand was added to the top of the resin, and then the column was filled with Milli-Q water above the bed volume. Acidified Milli-Q eluent (10 mL) was collected from the column to wash impurities from the sulfonated polystyrene beads and discarded. The Milli-Q water meniscus was brought down to the top of the bed volume prior to the addition of 5−10 mL of 0.25 M Na$_2$WO$_4$ solution. Five aliquots of the protonated H$_2$WO$_4$ solution were collected in 3 mL increments in standard scintillation vials. The solutions were allowed to stand overnight, during which time a yellow to yellow-green colloidal solution formed. H$_2$WO$_4$ colloidal solutions in highly acidic conditions are known to form yellowish isomorphous crystalline WO$_3$·2H$_2$O complexes.[30] Solutions of WO$_3$·2H$_2$O that produced well-defined and separated WO$_3$ nanodisk structures retained a creamy yellow color and did not become gelatinous. Other solutions with yellow-greenish colors and gelatinous properties were found to create aggregated nanodisk structures of poor quality (see Supporting Information). Next, three drops of the surfactant Triton X-100 and 0.0445 g of PEG-10000 were added to the colloidal solution of WO$_3$·2H$_2$O. PEG, ethylene glycol, and glycerol are known to form complexes with tungsten oxoanions and, consequently, to affect the conductivity in solution and the crystallinity and orientation in WO$_3$ thin films.[25,31] The WO$_3$·2H$_2$O/PEG-10000 solutions were then stirred overnight and stored in a 4 °C refrigerator.

Colloidal solutions were then dispersed onto conducting glass using a doctor blade method. The FTO conducting glass was initially cleaned with Milli-Q water, 2-propanol, methanol, and acetone and then allowed to dry while covered by a plastic Petri dish to avoid dust contamination. As a spacer, one layer of scotch tape was placed on the surface, and 50 μL of the WO$_3$·2H$_2$O/PEG-10000 solution was deposited across the entirety of the uncovered portion of the glass surface. Immediately after deposition, a clean glass rod was applied to the surface and swept forward and backward to remove excess colloidal solution. The film was briefly wafted and then covered with the Petri dish and allowed to dry. The spacers were then removed from the conducting substrate, and the thin film was sintered at 500 °C for 1−1.5 h with a Leister heat gun in open-air conditions.

WO$_3$ nanodisk electrodes were produced from a 1.25 cm by 1.25 cm FTO/WO$_3$ section of the as-prepared thin films. A

copper wire was attached to bare portions of the FTO conducting glass with silver conductive paint and allowed to dry thoroughly. Epoxy resin was then deposited on the glass surface to cover all uncoated FTO glass, the edges of the electrode, and most of the WO_3 thin film except for a rectangular window of exposed WO_3 nanodisk ca. 6 mm $\times$ 3 mm (0.18 cm^2) in area.

C. Morphology, Size, and Crystal Structure Characterization. SEM and HRSEM images were collected at the National Center for Electron Microscopy (NCEM) at Lawrence Berkeley National Laboratory on the FEI Strata 235 Dual Beam FIB (Focused Ion Beam) microscope and on a JEOL FESEM (field-emission scanning electron microscope). Accelerating voltages of 5−10 kV were employed for both microscopes. Sections of WO_3 thin films on FTO glass were placed on holders as-prepared without further preparation. TEM and HRTEM images were collected with a Phillips CM200/FEG (field-emission gun) microscope at NCEM as well. WO_3 nanodisks were placed onto Lacey Formvar 300-mesh carbon-coated copper grids by lightly pressing the grids against the surface of the thin film for approximately 1 min. XRD data were collected on a Bruker-AXS D8 instrument with a general area detector diffraction system (GADDS) and a Co Kα (1.79026 Å) radiation source. Data was obtained by placing the as-prepared WO_3 thin film onto the sample holder while focusing on areas of dense nanodisk populations found using SEM. AFM images were collected on a Pico LE SPM microscope (Molecular Imaging, Phoenix, AZ) using silica-etched tips. Data collection was performed on as-synthesized WO_3 nanodisks on the FTO substrate in tapping mode in air. Imaging was conducted at scans rates of 1−3 Hz with 256 $\times$ 256 pixel resolution. Raman scattering spectroscopy was performed on an RM series Renishaw microscope with a 50 mW diode laser at 780 nm. Renishaw's WiRE (Windows-based Raman Environment) proprietary software with Galactic Industries GRAMS/32 C software was used for data collection and analysis. WO_3 nanodisk thin films were visualized under white light, and then Raman scattering data were collected from 200 to 1500 cm^{-1}.

D. Photophysical and Electrochemical Characterization. UV−vis absorption spectroscopy was conducted on a Hewlett-Packard 8452A diode-array spectrophotometer (Palo Alto, CA). UV−vis spectra were measured by first placing a bare FTO glass substrate in the light path and subtracting the absorption pattern. Next, as-synthesized WO_3 nanodisk thin films on FTO substrates were measured to achieve an absorption spectrum of only the WO_3 nanodisks. CV was conducted on a CH Instruments 440 (Austin, TX) potentiostat with a working electrode of WO_3 nanodisks on a FTO substrate, a Pt wire counter electrode, and a Ag/AgCl reference electrode in a 0.5 M NaClO$_4$ electrolyte solution buffered to pH 4.43 with phosphate buffer. The measurements were conducted at a scan rate of 5 mV/s within a potential window ranging from +0.2 to −0.9 V. The electrolyte solution was stirred at 300 rpm and deaerated with N$_2$ for 20 min prior to the photoelectrochemistry experiments. All scans were conducted either in the dark or with UV illumination that was produced by a UVL-56 365-nm hand-held lamp (Upland, CA) without further modification.

3. Results

A. Ultrathin WO_3 Nanodisk Morphology, Size, and Crystal Structure. The surface-modulator-driven synthesis of WO_3 nanodisks using PEG-10000 (ca. 67 nm in length) was investigated by SEM and HRSEM. To properly determine the size range, a number of SEM images were examined (Figures 1−3). Figure 1A is a low-magnification SEM image of the WO_3
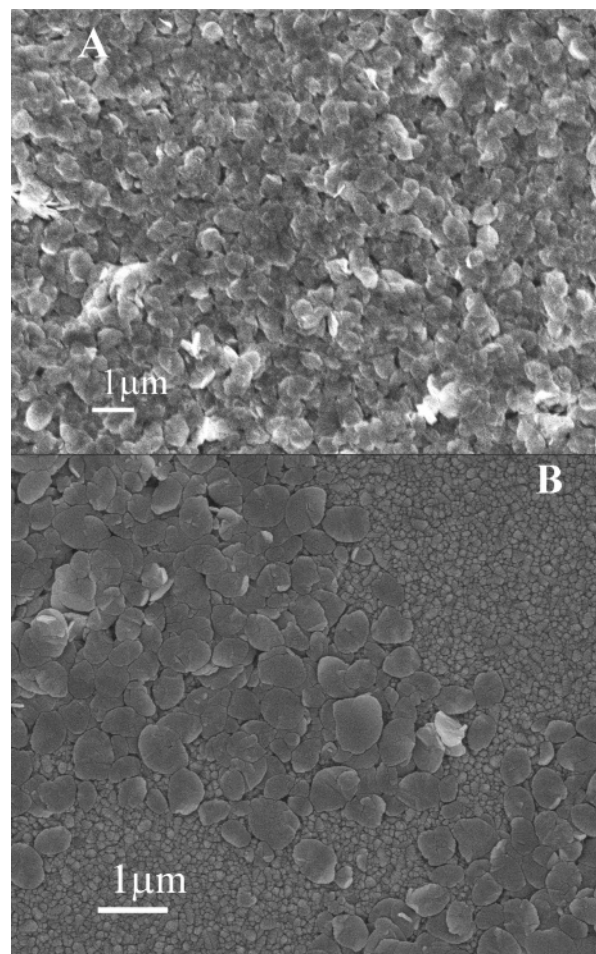
Figure 1. SEM images of WO_3 nanodisks. (A) A large population of nanodisks that lie atop one another in a thin film on a FTO substrate. (B) Higher-magnification image of less densely populated nanodisks showing their structures to range in size in the hundreds of nanometers along the long and short axes.

nanodisks in a dense cluster on the FTO substrate, and a vast majority of the nanodisks lie parallel to the surface. Disks lying normal to the surface are rare, but they appear white in the SEM image because of charging phenomena. Figure 1B shows a large number of individual nanodisks lying atop one another with a size range of 350−1000 nm along the long axis and 200−750 nm in the short axis. Low-resolution SEM images of a typical thin film edge were found to be ca. 0.5 μm in thickness after one application of the sol−gel method as described in the Materials and Methods section (not shown). Higher-magnification SEM images of the WO_3 nanodisks allowed for a better estimation of the size distribution inherent in this thin film system. Close examination of the ultrathin WO_3 structures revealed that individual nanodisks lying atop one another could be seen overlapping (Figure 2). The term "electron-transparent", usually reserved for thin TEM samples with small absorption cross sections, might be an appropriate description of the ability to see through these ultrathin WO_3 nanostructures. At higher magnifications, vertically oriented WO_3 nanodisks were examined and found to be ultrathin in comparison to the long and short axes of the structures (Figure 3). Figure 3A is especially interesting in that a nanodisk has a twinned crystal structure with a well-defined crystal hinge and a leading edge of ca. 500 nm in length and 12 nm in thickness. Figure 3B shows a nanodisk perpendicular to the surface with a long axis edge of over 450 nm (whole disk not captured in image) and a thickness of 17 nm. The extreme limit of thinness in the investigated

Ultrathin WO₃ Nanodisks Utilizing Long-Chain PEG

J. Phys. Chem. B, Vol. 110, No. 50, 2006 **25291**
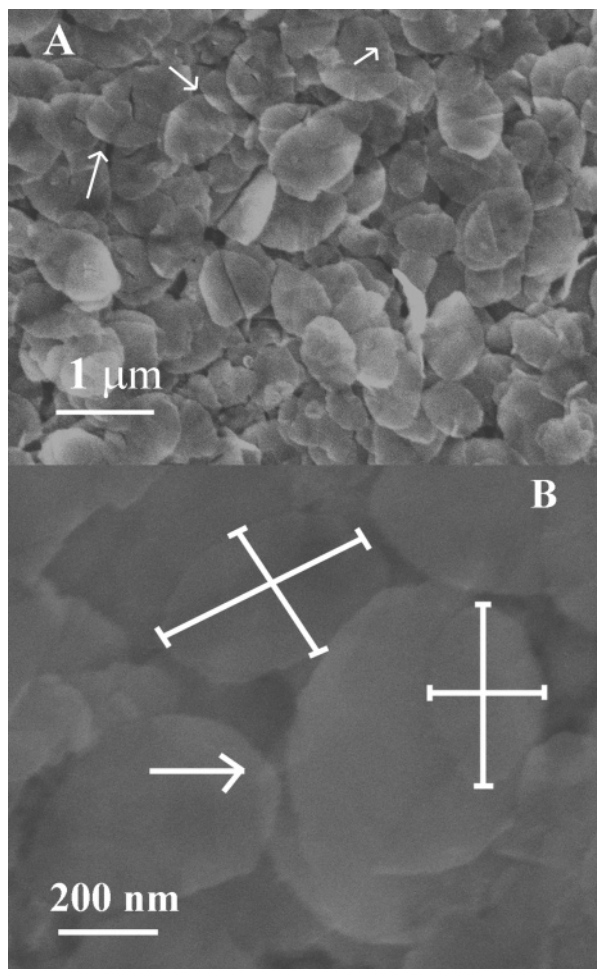
Figure 2. HRSEM images of WO₃ nanodisk thin films revealing the general size distribution of the nanodisks to be 350−1000 nm in length and 200−750 nm in width. Arrows in image A highlight regions where overlapping nanodisks show electron transparency in extremely thin samples. Crossbars in image B correspond to WO₃ nanodisks of 460 nm by 296 nm (top) and 373 nm by 230 nm. The arrow demarcates an area of four overlapping nanodisks and the edge effects that arise.

Figure 3. HRSEM images depicting vertically oriented WO₃ nanodisks and their thicknesses. (A) Twinned crystal with a thickness of 12 nm lodged between horizontally oriented nanodisks. (B) Nanodisk oriented normal to the FTO substrate showing extreme contrast of the nanodisks with a long axis of >500 nm and a thickness of 17 nm. (C) HRSEM image of a WO₃ nanodisk with a slight tilt at 1000K magnification exhibiting very small dimensions of 183 nm in length and a thickness of 6.7 nm on the far right edge. Measurements were taken at the solid white portions of the edge because of the tilt of the specimen and hazy characteristic of the trailing crystal face. The center edge highlighted by arrows was measured to be 10.5 nm in thickness.

system shows a slightly tilted nanodisk with a long axis of ca. 180 nm and a thickness of 6.7 nm (Figure 3C). Incidentally, the nanodisks that were vertically oriented and wedged were on the order of 200−500 nm on the measurable edge. Thus, the aspect ratios of the long axis to the thickness were ca. 20−30 from available data. Because of the lack of 500−1000-nm disks lying edge-on, it is difficult to determine the upper limit to these aspect ratios.

TEM of the WO₃ nanostructure reveals the disk to be prone to mechanical cracking when placed onto the Formvar carbon-coated copper grids (Figure 4). The textured single-crystalline WO₃ nanodisk with dimensions of 760 nm by 720 nm exhibits a number of breaks that result from the transfer process. Cracks and fractures of the nanodisk are located across whole portions of the single-crystalline areas and not along any crystal grain boundaries (Figure 4A). SAED (Figure 4B) of the WO₃ nanodisk gave a very uniform spot diffraction pattern of the monoclinic crystal phase with (101) and (202) crystal faces (JCPDS-#24-747). The nanodisk was lying parallel to the surface of the copper TEM grid, which allowed the determination that both the zone axis and inhibited crystal growth direction was [010]. Investigations into the crystal structure of the WO₃ nanodisks showed a generally uniform monoclinic phase and occasional lattice mismatching and vacancies (Figure 4C,D). The d spacings in Figure 4C were found to be 5.335 and 5.256

nm corresponding to (−101) and (101), respectively. The circular lightly shaded areas of Figure 4D had the most clear lattice spacing, and calculations for the four directions showed d spacings of 5.335, 5.256, 3.845, and 3.648 nm corresponding to the (−101), (101), (002), and (200) lattice planes, respectively. Closer inspection reveals the areas of textured single crystallinity and vacancies in the crystal lattice (Figure 4D). The stacking faults made d-spacing calculations difficult, and typically, these calculations could not be performed over 20 crystal lattice planes.

XRD of the as-prepared WO₃ thin films represent the monoclinic phase with large diffraction intensities of the (002), (120), and (−202) crystal faces (Figure 5). Most notably, the higher intensity of the (120) crystal face is quite unusual in comparison to traditional powder diffraction studies of monoclinic WO₃.[27] Spherical nanoparticles synthesized using low-molecular-weight PEG also showed large intensities for (200) and (020) and minute diffraction intensity for (120).[25] Preferentially oriented nanodisks with limited crystal faces satisfying the Bragg requirements might be a major contributor to this unorthodox distribution of diffraction peaks. The EDX spectrum displayed the representative peaks of oxygen and tungsten with a copper peak from the Formvar carbon-coated grid (Figure 6). The lack of any contamination confirms that all sodium ions were removed during the proton-exchange protocol to produce H₂WO₄ and that all carbon had been removed during the sintering process. AFM images of the nanostructures collected in tapping mode provided another confirmation of the size and morphology found by SEM and HRSEM. More importantly, the AFM data provided the ability to investigate the spatial separation of one nanodisk in relation to the others (Figure 7A,B). Utilizing the z-axis measurement tool allows the change in topography to be well characterized (bottom of Figure 7A,B). The WO₃ nanodisks at the surface were found to be at a slight tilt to the surface (~15°) of the FTO substrate instead of
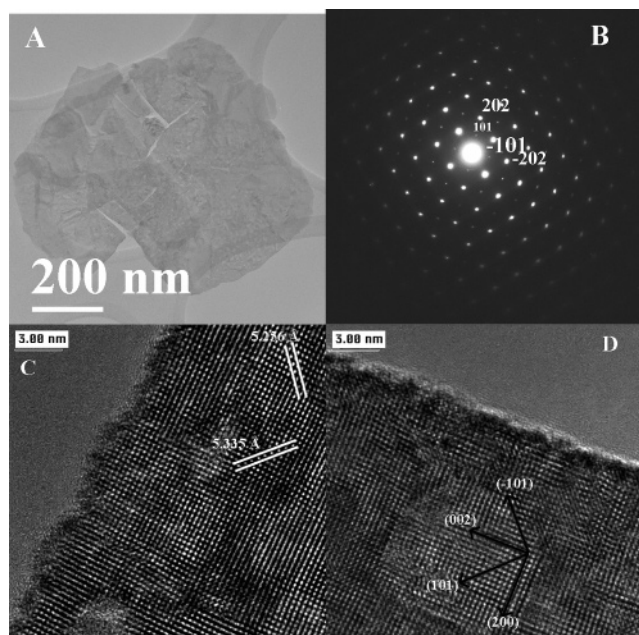
Figure 4. (A) TEM image of a 760 nm by 720 nm WO$_3$ nanodisk that cracked when transferred to the carbon-coated copper grid. The nanodisk is lying parallel to the surface, allowing for the examination of crystal growth directions. (B) Electron diffraction pattern showing a zone axis in the [010] direction and diffraction spots pertaining to the (202), (101), (−101), and (−202) crystal faces. HRTEM images of the WO$_3$ nanodisks reveal some vacancies and a textured single-crystalline nature. (C) Details of the *d* spacings of the monoclinic crystal phase of 5.335 and 5.253 nm corresponding to the (−101) and (101) crystal faces, respectively. (D) Whereas stacking faults were evident in the monoclinic WO$_3$ structure, the (−101), (101), (002), and (200) crystal planes were readily assigned and reinforced the SAED measurements.
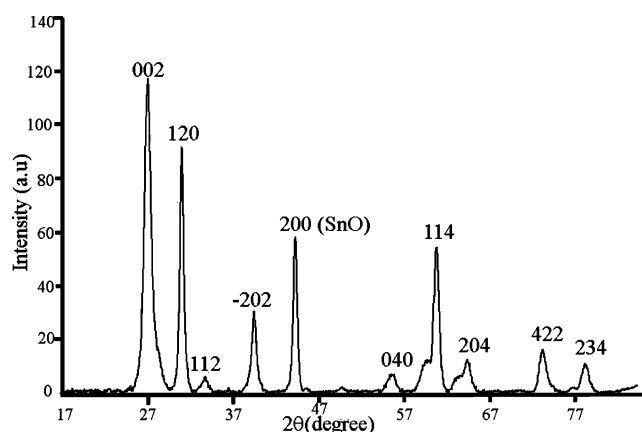
Figure 5. XRD data of WO$_3$ nanodisks with diffraction peaks corresponding to the (002), (120), and (−202) crystal faces and other lower-intensity diffraction peaks of the monoclinic phase. The unusually high diffraction intensity of the (120) peak is in large part due to the oriented WO$_3$ nanodisks lying nearly parallel to the FTO conducting substrate and the limited number of crystal faces satisfying Bragg's law.

perfectly parallel, as was originally thought. Above the array of overlaying nanodisks in Figure 7A,B are creased crystalline nanodisks. These crystal deformations were than attributed to the synthesis process and not to sample−tip interactions, which are extremely small in tapping-mode AFM. Raman scattering spectroscopy was also performed on the nanocrystalline WO$_3$ to probe the structural characteristics of the crystal phase. Vibrational modes at 713 and 804 cm^{-1} that coincide with the v(O−W−O) stretching modes of the monoclinic crystal phase
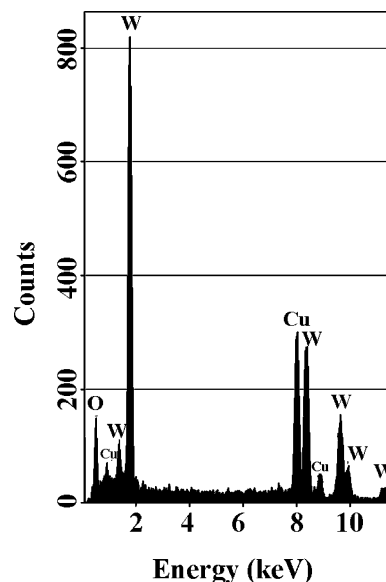
Figure 6. EDX spectra of WO$_3$ nanodisks on Formvar carbon-coated copper grids displaying the compositional peaks of oxygen and tungsten. Copper peaks due to the copper grid were also identified. No peaks corresponding to carbon were present, indicating that all of the PEG-10000 was removed during the sintering process.

were present (Figure 8A).[32] The spectrum of the WO$_3$ nanodisks was taken at room temperature after 1 h of sintering at 500 °C with a heat gun. Raman spectra of a WO$_3$ thin film that had been sintered at 700 °C in a furnace showed massive increases in Raman intensity and additional vibrational modes at 283 and 320 cm^{-1}, which correspond to the bending modes of δ(O−W−O) (Figure 8B).[32] Structurally, the WO$_3$ nanodisks dissolved at high temperatures and became primarily spheres, with sporadic growth of WO$_3$ nanorods and microplate structures (see Supporting Information). We believe that the high surface area and increased scattering of the WO$_3$ nanodisks contributed to the low signal-to-noise ratio. Differences in the two spectra are attributed mainly to the higher crystallinity of the WO$_3$ nanoparticles and a larger density of available nanoparticles in the laser beam area.

B. Optical and Electrochemical Characterization. UV−vis absorption spectroscopy was performed on WO$_3$ nanodisk thin films with and without subtraction of the absorption of the FTO substrate (Figure 9). Peaks at 200 and 290 nm are due solely to the absorption of the FTO conducting glass. After blanking, the absorption profile of the WO$_3$ nanodisks revealed a prominent peak at 320 nm (3.8 eV), a shoulder at 490 nm (2.5 eV), and then continued absorption into the IR region. Blue shifting of the band gap energy from 440 nm (2.8 eV) might be due, in part, to size quantization effects of the ultrathin nanostructures, whereas absorption in the 400−500 nm is typical of WO$_3$ thin films.[33] As far as 740 nm (1.7 eV), the absorption of the WO$_3$ nanodisks was 0.1 (80% transmittance) and might be a product of scattering of the planar WO$_3$ nanodisks. Absorption of the WO$_3$ nanodisks into the IR range is unusual in comparison to both bulk and nanocrystalline WO$_3$ systems, for which the absorption profiles end at 500 nm.[20,21,34,35] The lack of absorption in the thin film below 320 nm is an experimental artifact resulting from the blanking process and could be corrected with the use of an integrating sphere.

Electrochemical measurements of the WO$_3$ nanodisks were conducted in buffered electrolyte solutions in the dark and with a handheld UV lamp at pH 4.43. WO$_3$ resistance to photocorrosion in acidic conditions makes WO$_3$ a quality candidate for
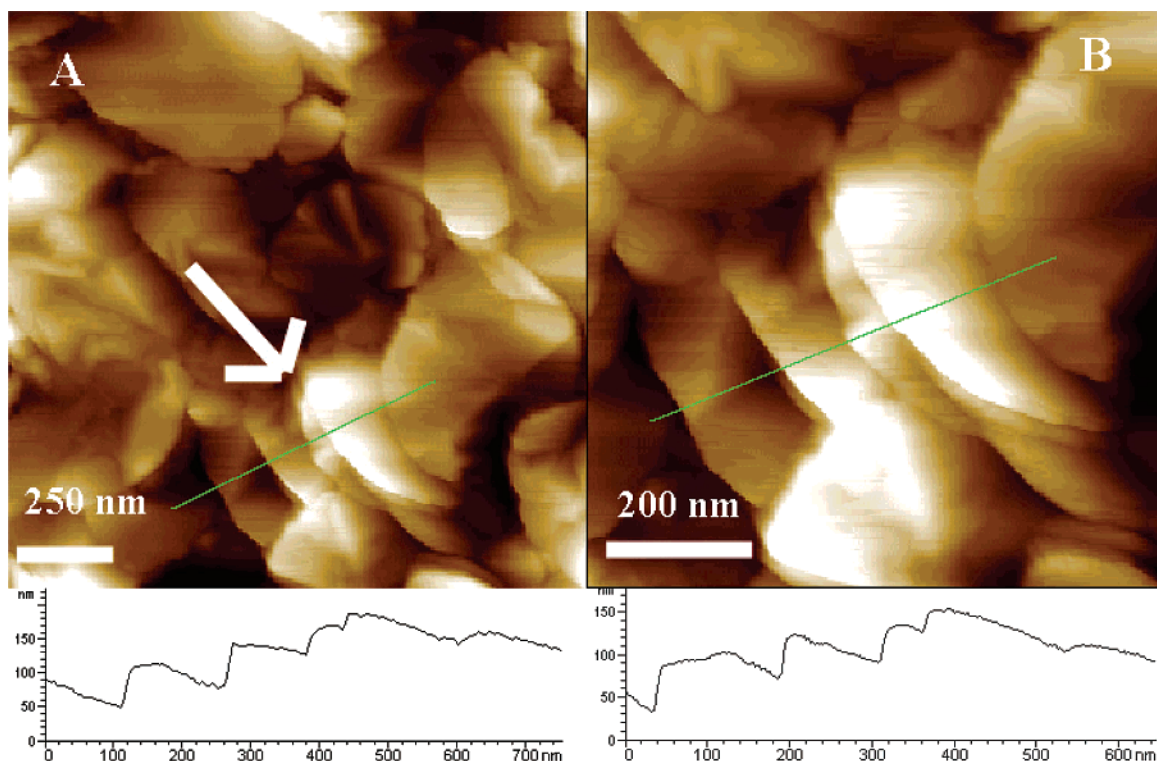
Figure 7. AFM images in tapping mode with silica-etched tips of the WO$_3$ nanodisks. (A) General scan with a stacked formation of nanodisks; the arrow indicates the area magnified in B. Based on the *z*-axis measurement tool (lower parts of A and B), the nanodisks were believed to have been 30−40 nm in thickness, which was later contradicted by the HRSEM data. Image B is a close-up of the stacked WO$_3$ nanodisk array, revealing the close proximity of the nanodisks to one another. It also indicates that the disks are not lying perfectly parallel to the ITO substrate, but are, in fact, at a slight angle of ca. 15°.

photoelectrochemical cells.[29] CV data were collected at a scan rate of 5 mV/s within a potential window between +0.2 and −0.6 V (Figure 10A). A cathodic peak at −0.4 V and an anodic peak at −0.2 V were observed with and without UV light exposure (Figure 10A). These cathodic and anodic peaks have been assigned to the intercalation and deintercalation of H$^+$ and Na$^+$ ions into the WO$_3$ thin film.[21] The ca. 50% increase of the cathodic and anodic currents during UV illumination can be attributed to a photocurrent generated from photoexcited electron−hole pairs.[33] The CV data in Figure 10B were acquired in a potential window between +0.2 and −0.9 V and revealed several cathodic and anodic peaks in the dark. Cathodic twin peaks were observed at −0.4 and −0.48 V, and a broad shoulder can also be seen at −0.8 V. The double peaks around −0.4 V are again attributed to H$^+$ and Na$^+$ intercalation, but the twinning is speculated to relate to the various sizes of the WO$_3$ nanodisks and is not completely understood at this point. The shoulder at −0.8 V is assigned to the electrochemical reduction of H$^+$ to gaseous H$_2$ at the WO$_3$ electrode.[36] Lack of an anodic peak at −0.8 V is representative of the irreversibility of the reaction once H$_2$ gas escapes the system. Outside the potential windows usually associated with electrochromic WO$_3$, H$_2$ evolution has been documented at higher negative potentials, but it should be noted that damage can occur during H$^+$/H$_2$ reduction.[36] The anodic peaks in the dark are also twinned, with peaks at −0.2 and −0.3 V, and are believed to arise from the deintercalation of H$^+$ and Na$^+$ ions from the WO$_3$ crystal lattice, with speculation that the nanodisk size heterogeneity might be the cause. Under UV illumination, the twinned cathodic peaks were averaged to a single peak at ca. −0.42 V, and an increase in current of ca. −18.5 μA/cm^2 was observed (60% increase compared to that in the dark). The anodic peaks retained their twinned character under UV illumination, but shifted to more

negative potentials of −0.24 and −0.36 V. Again, we saw an increase in current of both peaks, but an especially large increase was observed for the −0.24 V peak from 9 to 18 μA/cm^2 (100% increase).

4. Discussion

A. Ultrathin WO$_3$ Nanodisk Growth Mechanism, Size, and Orientation. Surfactant- and surface-modulator-driven synthesis of nanomaterials is being vastly exploited because of the inherent changes in optical, electronic, and magnetic properties at the nanoscale.[37] Here, the use of high-molecular-weight PEG-10000 with an approximate length of 67 nm aids in the formation of highly planar and well-separated WO$_3$ nanodisks. PEG of low molecular weight was extensively studied in a tungstic acid system very similar to ours and was shown to not only orient crystal growth, but also facilitate a metastable hexagonal WO$_3$ crystal structure.[25] When Choi et al. introduced PEG-6000 into their tungstic acid system, they achieved stacked platelets of monoclinic WO$_3$, but did not present a mechanism for the formation of the structures.[26]

Here, we propose that the formation of the WO3 nanodisks is driven by the preferential adsorption of PEG-10000 onto the (010) crystal face, thereby inhibiting crystallographic growth. Directed growth of Co nanodisks and CdTe tetrapods exploit this adsorption of molecules such as alkylamines and phosphonic acids to certain crystal faces with great success.[38,39]

After the proton exchange of Na$_2$WO$_4$ to H$_2$WO$_4$ and formation of WO$_3$·2H$_2$O crystallites in solution, PEG-10000 forms a complex with the crystallites directly. The nature of the nonionic surfactant Triton X-100, C$_{14}$H$_{22}$O(C$_2$H$_4$O)$_9$, in the solution is not completely clear, but its hydrophilic moieties can also complex with WO$_3$·2H$_2$O in a similar fashion. Use of
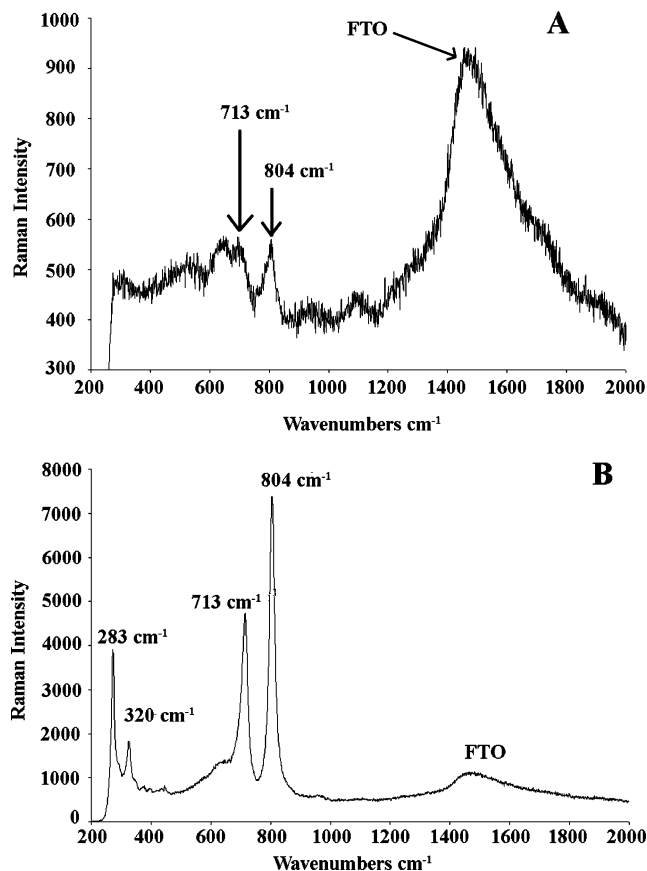
Figure 8. Raman spectra of WO$_3$ nanodisk thin films taken at room temperature showing the vibrational modes associated with the monoclinic phase. (A) WO$_3$ nanodisks sintered at 500 °C and confirmed by HRSEM prior to Raman spectroscopy. They show the 804 and 713 cm^{-1} vibrational modes that correspond to v(O−W−O) stretching along with vibrational modes at 1500 cm^{-1} from the FTO conducting glass. (B) WO$_3$ thin film sintered at 700 °C in a furnace that was determined by HRSEM to have become nanospheres and nanorods (see Supporting Information). It has increased Raman scattering intensity and additional stretching modes at 283 and 320 cm^{-1} that are representative of the v(O−W−O) bending modes.

Triton X-100 with addition of PEG-600, PEG-1000, and PEG-2000 leads to structures of spherical nanoparticles[21] and globular/spheroid nanostructures, respectively. Therefore, it seems reasonable to conclude that PEG-10000 is a driving force in producing such ultrathin structures. The PEG used in this study has an average molecular weight of 10000 g/mol, but has an actual molecular weight range of 8500−11500 g/mol (57−77 nm) and might contribute to the size distribution of the WO$_3$ nanodisks. Further size narrowing of the long-chain PEG in size-exclusion columns might aid in producing more homogeneous distributions of WO$_3$ nanodisks.

SEM and HRSEM of the WO$_3$ nanodisks showed the nanostructures to be polydispersed with lengths of 350−1000 nm, widths of 200−750 nm, and thicknesses of 7−18 nm (Figures 1−3). Investigations of WO$_3$ phase transitions based on temperature indicate the following trend: triclinic (∼30 °C) → monoclinic (330 °C) → orthorhombic (740 °C) → tetragonal.[40] We propose that, while the tungsten precursors are in their triclinic crystal phase, PEG-10000 adsorbs to the (010) crystal face. Because the decomposition of PEG does not occur until ca. 350 °C, WO$_3$ nanodisks had already entered into the triclinic → monoclinic phase transition prior to the complete combustion of PEG from the thin film. EDX spectra did not show any representative peaks for carbon, and so, complete removal of the surface modulator is evident (Figure 6). Close interactions
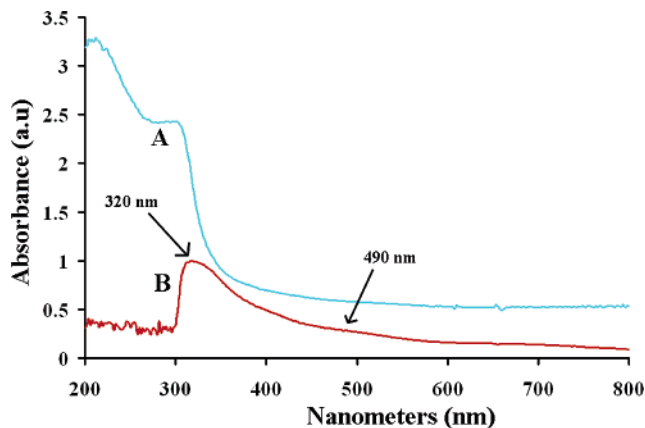
Figure 9. UV−vis absorption spectra of solutions of WO$_3$ thin films. (A) Spectrum recorded without blanking of the FTO substrate prior to data collection showing pronounced absorption peaks at 200 and 290 nm and absorption extending into the IR range. (B) Spectrum recorded after blanking of the FTO substrate prior to data collection showing a very sharp peak at 320 nm and absorption extending into the IR range. The IR absorbance is attributed to scattering due to the large surface area of the WO$_3$ nanodisks. The 200−300-nm region of spectrum B is an artifact due to blanking.
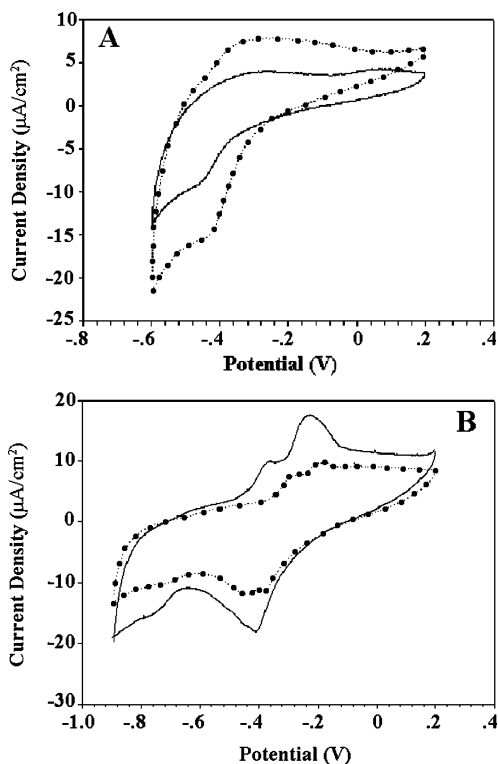
Figure 10. Cyclic voltammograms were performed in the range from +0.2 to −0.9 V at a 5 mV/s scan rate on WO$_3$ nanodisk electrodes in 0.5 M Na$_2$ClO$_4$ buffered with phosphate buffer at pH 4.43 and a Ag/AgCl reference electrode. (A) CV data showing a cathodic peak at −0.4 V and an anodic peak at −0.2 V assigned to the intercalation and deintercalation of H$^+$ and Na$^+$ ions in the dark (• - • -) and under UV illumination (−). (B) CV data collected in a potential window between +0.2 V and −0.9 V revealing a set of split anodic and cathodic peaks in the dark (• - • -) perhaps due to size differences in nanodisks. Under UV illumination (−), an increase in current is observed, a shift is seen in the anodic peaks to higher negative potentials, and the cathodic peaks merge to a single peak at −0.4 V.

of the WO$_3$·2H$_2$O/PEG-10000 system resulted in WO$_3$ nanodisks ranging from 9 unit cells thick (∼6.7 nm) to 24 unit cells thick (∼18 nm) in the [010] crystal direction. The relatively large aspect ratios (length-to-thickness ratios) of the nanodisks,

Ultrathin WO₃ Nanodisks Utilizing Long-Chain PEG

J. Phys. Chem. B, Vol. 110, No. 50, 2006 **25295**

with values of 20−30, support our PEG adsorption model of how such large-surface-area nanostructures could simultaneously attain crystallinity and extreme thinness. The lack of large nanodisks (500−1000 nm) lying normal to the FTO substrate reinforces the conclusion that the PEG molecules lie fairly parallel to the surface as well as adsorbing to the (010) crystal face. Only a minority of interspersed WO₃ nanodisks attain a vertical orientation, primarily by being wedged between collections of larger nanodisks (Figure 3).

The WO₃ crystal was found to have a textured single-crystalline structure with primarily good crystal lattice profiles and few vacancies (Figures 4). Originally, the nanodisks were believed to have been amorphous because of their curved edges and rose-petal-like morphologies (Figure 1). XRD data collected from the WO₃ nanodisk thin film showed strong diffraction intensities for the (002), (120), and (−202) crystal faces largely attributed to the planar orientation of the structures in comparison to thin films of spherical WO₃ nanoparticles reported in previous studies (Figure 5).[21] The unusually large peak corresponding to the (120) crystal face supports the conclusion that crystal growth was permitted in only certain directions. This system of highly planar, large-surface-area WO₃ nanodisks could have enhanced electron-transport characteristics compared to thin films of WO₃ nanoparticles.[41] SAED of a single nanodisk that had been cracked in several areas during deposition onto the copper grid showed excellent spot diffraction characteristics of monoclinic WO₃ (Figure 4). Difficulties in finding single intact nanodisks hindered the collection of clear electron diffraction patterns because of the propensity of two or three nanodisks to lie atop one another after transfer. The cracking of the nanodisk attested to their crystalline nature and also to their fragility (Figure 4). Investigations of the individual nanodisks as probed by AFM showed tilted orientations relative to the FTO substrate (Figure 7). The *z*-axis height tool showed their close proximity to one another while orienting themselves in a tile-roof-like fashion. The WO₃ nanodisks on the surface had angles of ca. 15° (Figure 7), but removal of nanodisks through contact-mode AFM could reveal more parallel orientations of underlying nanodisks. This, of course, is not an upper limit to the allowed tilting, as was seen previously with vertically oriented nanodisks in small numbers. The high porosity of the WO₃ nanodisks seen through AFM should lead to efficient sensitizing of the thin films by polymers or quantum dots for increased light-harvesting capabilities.

B. WO₃ Nanodisk Structure as an Intermediate Phase. Owing to drastic changes in morphology at higher calcination temperatures, we believe the WO₃ nanodisks to be a metastable structure. During the probing into the appropriate calcination temperature, we found that the nanodisks would ultimately dissolve into nanospheres and nanorods at temperatures of 700 °C in a furnace (Supporting Information). The dramatic change in morphology can be attributed to a thermodynamic limitation to the stability of the nanodisks. Nanosphere structures previously reported with low-molecular-weight PEG and calcination at 500 °C were analogous to the structures seen at elevated temperatures here.[29] Nanorod formation in sparse populations was also apparent and likened to the growth of vapor-deposited WO₃ nanorods/nanobelts at temperatures of 950−1000 °C with pure tungsten filaments in air.[42] We believe that the limited nanorod formation was due to hot spots in the FTO substrate and that increased temperatures would enhance nanorod formation.

Raman scattering spectroscopy showed dramatic changes in intensity between WO₃ nanodisks and nanospheres (Figure 8).

Raman spectroscopy was key in originally characterizing the monoclinic WO₃ structure through weak Raman signals at 713 and 804 cm⁻¹ corresponding to the stretching modes, υ(O−W−O). The Raman spectra of the nanodisks changed dramatically after calcination at 700 °C. Most notable are the rise of the bending mode, δ(O−W−O), at 283 and 320 cm⁻¹ and the order-of-magnitude increase of the stretching mode intensity. We attribute the differences to the increased scattering of the large-surface-area WO₃ nanodisks and smaller inherent population per unit area of the thin film. Higher populations of WO₃ nanospheres interacting with the laser radiation and random orientation could be a contributing factor to their strong Raman spectra.

C. Photophysical and Photoelectrochemical Properties. UV−visible absorption spectra of WO₃ thin films have a pronounced peak at 320 nm (3.8 eV), far blue-shifted from the band gap energy of 2.8 ev (440 nm), and trailing IR absorption. Bedja et al. found a similar quantized effect with 2.0−5.0-nm WO₃ nanospheres prepared with oxalic acid and an absorption at 380 nm (3.3 eV). The absorbance profile might be a consequence of the confined nature of the electrons in the [010] direction, but no investigations have adequately explained the results spectroscopically. The lack of absorbance below 320 nm is an experimental artifact due to the blanking process and could be corrected with an integrating-sphere absorption measurement. The apparent absorption into the IR range is attributed to the scattering of the WO₃ nanodisk and is reasonable considering the near-micrometer scale of the examined system parallel to the FTO substrate.

From CV studies in NaClO₄ electrolyte solution at pH 4.43, the WO₃ nanodisk electrode was found to be robust after multiple runs and did not decay in the acidic solution. Whereas the gaseous evolution of H₂ appeared to be very weak at very negative potentials with UV illumination (above −0.8 V), the ability to reduce H⁺/H₂ at the WO₃ surface is documented outside of the potential window usually associated with WO₃ electrochromic behavior.[35,36] Hydrogen evolution is considered the limiting potential of the WO₃ electrode in its electrochromic properties and would inhibit its use as an electrochromic window.[36] The twinning of the anodic and cathodic peaks in Figure 10B shows characteristics that the various sizes of the nanodisks might play a role. Narrowing of the WO₃ nanodisk size distribution might further clarify this hypothesis and lead to a sharper set of cathodic and anodic peaks. An increased current of 50−100% from electron−hole pairs generated by UV light is reasonable, but the quality and increased thickness (ca. 0.5 μm) of the films might produce better results with better charge separation at the electrode−electrolyte interface. These preliminary studies are a test of the photoelectrochemical parameters, but additional studies of photocurrent and action spectra with monochromatic light are to follow.

5. Conclusion

Ultrathin WO₃ nanodisks have been synthesized using PEG-10000 as a surface modulator that adsorbs preferentially to the (010) crystal face and thereby inhibits crystal growth. The nanodisk formation is critically influenced by the interaction between PEG and the WO₃·2H₂O precursors as compared to other studies resulting in spherical nanoparticles. The nanodisks were carefully characterized using a combination of experimental techniques including TEM, SEM, AFM, XRD, EDX, Raman scattering spectroscopy, UV−visible spectrophotometry, and CV. The large flat surface area, high aspect ratio, and textured single crystallinity of the WO₃ nanodisks could have

Wolcott et al.

enhanced charge-transport properties compared to WO_3 nanoparticles. The examination into nanodisk structures is a natural transition for thin film investigations after 0-D and 1-D nanostructures and might prove beneficial. They are potentially useful in a number of applications including photovoltaics, photocatalysis, and photoelectrochemistry.

Supporting Information Available: (A) SEM image of aggregated WO_3 nanodisks from contaminated $WO_3 \cdot H_2O$/PEG solutions, (B) SEM image of spherical WO_3 nanoparticles and WO_3 plate after sintering at 700 °C in a furnace, (C) WO_3 nanorod growth from a layer of WO_3 nanoparticles. This material is available free of charge via the Internet at http://pubs.acs.org.

References and Notes

(1) Brook, E. J. *Science* **2005**, *310*, 1285.
(2) Turner, J. A. *Science* **1999**, *285*, 687.
(3) Khaselev, O.; Turner, J. A. *Science* **1998**, *280*, 425.
(4) Gratzel, M. *Nature* **2001**, *414*, 338.
(5) Lewis, N. S.; Crabtree, G. W.; Nozik, A. J.; Wasielewski, M. R.; Alivisatos, A. P. *Basic Research Needs for Solar Energy Utilization: Report of the Basic Energy Sciences Workshop on Solar Energy Utilization*; Office of Sciences, U.S. Department of Energy, U.S. Government Printing Office: Washington, DC, 2005; p 1.
(6) Hagfeldt, A.; Gratzel, M. *Acc. Chem. Res.* **2000**, *33*, 269.
(7) Chandrasekharan, N.; Kamat, P. V. *J. Phys. Chem. B* **2000**, *104*, 10851.
(8) Park, J. H.; Bard, A. J. *Electrochem. Solid State Lett.* **2005**, *8*, G371.
(9) Keis, K.; Magnusson, E.; Lindstrom, H.; Lindquist, S. E.; Hagfeldt, A. *Solid State Lett.* **2002**, *73*, 51.
(10) Lindgren, T.; Wang, H. L.; Beermann, N.; Vayssieres, L.; Hagfeldt, A.; Lindquist, S. E. *Solid State Lett.* **2002**, *71*, 231.
(11) Law, M.; Greene, L. E.; Johnson, J. C.; Saykally, R.; Yang, P. D. *Nat. Mater.* **2005**, *4*, 455.
(12) Jiu, J. T.; Isoda, S.; Wang, F. M.; Adachi, M. *J. Phys. Chem. B* **2006**, *110*, 2087.
(13) Yu, Z. G.; Pryor, C. E.; Lau, W. H.; Berding, M. A.; MacQueen, D. B. *J. Phys. Chem. B* **2005**, *109*, 22913.
(14) Han, W. Q.; Fan, S. S.; Li, Q. Q.; Hu, Y. D. *Science* **1997**, *277*, 1287.
(15) Jin, R. C.; Cao, Y. W.; Mirkin, C. A.; Kelly, K. L.; Schatz, G. C.; Zheng, J. G. *Science* **2001**, *294*, 1901.
(16) Murray, C. B.; Norris, D. J.; Bawendi, M. G. *J. Am. Chem. Soc.* **1993**, *115*, 8706.
(17) Gaponik, N.; Talapin, D. V.; Rogach, A. L.; Hoppe, K.; Shevchenko, E. V.; Kornowski, A.; Eychmuller, A.; Weller, H. *J. Phys. Chem. B* **2002**, *106*, 7177.
(18) Nozik, A. J. *Inorg. Chem.* **2005**, *44*, 6893.
(19) Ramana, C. V.; Utsunomiya, S.; Ewing, R. C.; Julien, C. M.; Becker, U. *J. Phys. Chem. B* **2006**, *110*, 10430.
(20) Santato, C.; Ulmann, M.; Augustynski, J. *Adv. Funct.* **2001**, *13*, 511.
(21) Wang, H. L.; Lindgren, T.; He, J. J.; Hagfeldt, A.; Lindquist, S. E. *J. Phys. Chem. B* **2000**, *104*, 5686.
(22) Li, Y. B.; Bando, Y.; Golberg, D.; Kurashima, K. *Chem. Phys. Lett.* **2003**, *367*, 214.
(23) Satishkumar, B. C.; Govindaraj, A.; Nath, M.; Rao, C. N. R. *J. Mater. Chem.* **2000**, *10*, 2115.
(24) Zou, G. F.; Xiong, K.; Jiang, C. L.; Li, H.; Wang, Y.; Zhang, S. Y.; Qian, Y. T. *Nanotechnology* **2005**, *16*, 1584.
(25) Santato, C.; Odziemkowski, M.; Ulmann, M.; Augustynski, J. *J. Am. Chem. Soc.* **2001**, *123*, 10639.
(26) Choi, Y. G.; Sakai, G.; Shimanoe, K.; Yamazoe, N. *Sens. Actuators B: Chem.* **2004**, *101*, 107.
(27) Loopstra, B. O.; Boldrini, P. *Acta Crystallogr. B* **1966**, *21*, 158.
(28) Yumashev, K. V.; Malyarevich, A. M.; Posnov, N. N.; Denisov, I. A.; Mikhailov, V. P.; Artemyev, M. V.; Sviridov, D. V. *Chem. Phys. Lett.* **1998**, *288*, 567.
(29) Santato, C.; Ulmann, M.; Augustynski, J. *J. Phys. Chem. B* **2001**, *105*, 936.
(30) Cotton, F. A., Wilkinson, G. *Advanced Inorganic Chemistry*, 3rd ed.; Interscience Publishers: New York, 1972.
(31) Richardson, E. *J. Inorg. Nucl. Chem.* **1959**, *12*, 79.
(32) Daniel, M. F.; Desbat, B.; Lassegues, J. C.; Gerand, B.; Figlarz, M. *J. Solid State Chem.* **1987**, *67*, 235.
(33) Bedja, I.; Hotchandani, S.; Kamat, P. V. *J. Phys. Chem.* **1993**, *97*, 11064.
(34) Reichman, B.; Bard, A. J. *J. Electrochem. Soc.* **1979**, *126*, 2133.
(35) Spichigerulmann, M.; Augustynski, J. *J. Appl. Phys.* **1983**, *54*, 6061.
(36) Shen, P.; Tseung, A. C. C. *J. Mater. Chem.* **1994**, *4*, 1289.
(37) Puntes, V. F.; Krishnan, K. M.; Alivisatos, A. P. *Science* **2001**, *291*, 2115.
(38) Manna, L.; Milliron, D. J.; Meisel, A.; Scher, E. C.; Alivisatos, A. P. *Nat. Mater.* **2003**, *2*, 382.
(39) Puntes, V. F.; Zanchet, D.; Erdonmez, C. K.; Alivisatos, A. P. *J. Am. Chem. Soc.* **2002**, *124*, 12874.
(40) Cazzanelli, E.; Vinegoni, C.; Mariotto, G.; Kuzmin, A.; Purans, J. *Solid State Ionics* **1999**, *123*, 67.
(41) Bedja, I.; Hotchandani, S.; Carpentier, R.; Vinodgopal, K.; Kamat, P. V. *Thin Solid Films* **1994**, *247*, 195.
(42) Jin, Y. Z.; Zhu, Y. Q.; Whitby, R. L. D.; Yao, N.; Ma, R. Z.; Watts, P. C. P.; Kroto, H. W.; Walton, D. R. M. *J. Phys. Chem. B* **2004**, *108*, 15572.